The Journal of Experimental Biology 206, 327-343

doi:10.1242/jeb.00069

The hydrodynamics of locomotion at intermediate Reynolds numbers: undulatory swimming in ascidian larvae (*Botrylloides* sp.)

Matthew J. McHenry[1,*], Emanuel Azizi[2] and James A. Strother[1]

[1]*Department of Integrative Biology, University of California, Berkeley, CA 94720, USA* and [2]*Organismic and Evolutionary Biology Program, 221 Morrill Science Center, University of Massachusetts, Amherst, MA 01003, USA*

*Author for correspondence at present address: The Museum of Comparative Zoology, Harvard University, 26 Oxford St, Cambridge, MA 02138, USA (e-mail: mchenry@fas.harvard.edu)

Accepted 10 October 2002

Summary

Understanding how the shape and motion of an aquatic animal affects the performance of swimming requires knowledge of the fluid forces that generate thrust and drag. These forces are poorly understood for the large diversity of animals that swim at Reynolds numbers (*Re*) between 10^0 and 10^2. We experimentally tested quasi-steady and unsteady blade-element models of the hydrodynamics of undulatory swimming in the larvae of the ascidian *Botrylloides* sp. by comparing the forces predicted by these models with measured forces generated by tethered larvae and by comparing the swimming speeds predicted with measurements of the speed of freely swimming larvae. Although both models predicted mean forces that were statistically indistinguishable from measurements, the quasi-steady model predicted the timing of force production and mean swimming speed more accurately than the unsteady model. This suggests that unsteady force (i.e. the acceleration reaction) does not play a role in the dynamics of steady undulatory swimming at $Re \approx 10^2$. We explored the relative contribution of viscous and inertial force to the generation of thrust and drag at $10^0 < Re < 10^2$ by running a series of mathematical simulations with the quasi-steady model. These simulations predicted that thrust and drag are dominated by viscous force (i.e. skin friction) at $Re \approx 10^0$ and that inertial force (i.e. form force) generates a greater proportion of thrust and drag at higher *Re* than at lower *Re*. However, thrust was predicted to be generated primarily by inertial force, while drag was predicted to be generated more by viscous than inertial force at $Re \approx 10^2$. Unlike swimming at high ($>10^2$) and low ($<10^0$) *Re*, the fluid forces that generate thrust cannot be assumed to be the same as those that generate drag at intermediate *Re*.

Key words: swimming, intermediate Reynolds number, morphology, larvae, ascidian, urochordata, *Botrylloides* sp.

Introduction

Understanding how the shape and motion of an aquatic animal affects the performance of swimming requires knowledge of the fluid forces that generate thrust and drag. Despite recent advances towards understanding the biomechanics of locomotion (see Dickinson et al., 2000 for a review), these forces are poorly understood in swimming animals that are a few millimeters in length. The large diversity of larval fish and marine invertebrates at this scale generate hydrodynamic force that is dependent on both the viscosity and the inertia of the surrounding water. To understand the relative contribution of inertial and viscous forces to the generation of thrust and drag, theoretical models have been developed for the hydrodynamics of swimming at this scale (e.g. Jordan, 1992; Vlyman, 1974; Weihs, 1980). However, little experimental work has attempted to test or refine these theories (exceptions include Fuiman and Batty, 1997; Jordan, 1992). The goal of the present study was to test hydrodynamic theory by comparing the predictions of theoretical models with measurements of the speed of freely swimming animals and the forces generated by tethered animals.

Swimmers that are millimeters in length generally operate in a hydrodynamic regime characterized by Reynolds numbers (*Re*) between 10^0 and 10^3, which is a range referred to as the intermediate *Re* in the biological literature (e.g. Daniel et al., 1992). *Re* ($Re=\rho\bar{u}L/\mu$, where $\bar{u}$ is mean swimming speed, L is body length, ρ is density of water, and μ is dynamic viscosity of water) approximates the ratio of inertial to viscous forces and suggests how much different fluid forces contribute to propulsion. At intermediate *Re*, a swimming body may experience three types of fluid force: skin friction, form force and the acceleration reaction. Skin friction and form force are quasi-steady and therefore vary with the speed of flow. In previous studies on intermediate *Re* swimming, these forces have collectively been referred to as the ‘resistive force’ (e.g. Jordan, 1992). However, we will consider these forces separately because the present study is concerned with how

they individually contribute to the generation of thrust and drag.

Skin friction is generated by the resistance of fluid to shearing. This is a viscous force, which means that it increases in proportion to the speed of flow. Skin friction (also called the 'resistive force' by Gray and Hancock, 1955) dominates the undulatory swimming of spermatozoa ($Re \ll 10^0$; Gray and Hancock, 1955) and nematodes (Gray and Lissmann, 1964) and has been hypothesized to contribute to thrust and drag in the intermediate *Re* swimming of larval fish (Vlyman, 1974; Weihs, 1980) and chaetognaths (Jordan, 1992).

The form force is generated by differences in pressure on the surface of the body and it varies with the square of flow speed (Granger, 1995). This inviscid force is equivalent to the resultant of steady-state lift and drag acting on a body at $Re > 10^3$. The form force is thought to contribute to the generation of thrust and drag forces at the intermediate *Re* swimming of larval fish (Vlyman, 1974; Weihs, 1980) and may dominate force generation by the fins of adult fish (Dickinson, 1996).

The acceleration reaction [also referred to as the 'reactive force' (Lighthill, 1975), the 'added mass' (Nauen and Shadwick, 1999) and the 'added mass inertia' (Sane and Dickinson, 2001)] is generated by accelerating a mass of water around the body and is therefore an unsteady force (Daniel, 1984). This force plays a negligible role in the hydrodynamics of swimming by paired appendages at $Re < 10^1$ (Williams, 1994) but is considered to be important to undulatory swimming at intermediate *Re* (Brackenbury, 2002; Jordan, 1992; Vlyman, 1974) and dominant in some forms of undulatory swimming at $Re > 10^3$ (Lighthill, 1975; Wu, 1971). Although it is assumed that the acceleration reaction does not play a role in undulatory swimming at $Re < 10^0$ (Gray and Hancock, 1955), it is not understood how the magnitude of the acceleration reaction varies across intermediate *Re*.

Weihs (1980) proposed a hydrodynamic model that predicted differences in the hydrodynamics of undulatory swimming in larval fish at different intermediate *Re*. He proposed a viscous regime at $Re < 10^1$, where viscous skin friction dominates propulsion, and an inertial regime at $Re > 2\times10^2$, where inertial form force and the acceleration reaction are dominant (also see Weihs, 1974). For the range of *Re* between these domains, thrust and drag were hypothesized to be generated by a combination of skin friction, form force and the acceleration reaction. Although frequently cited in research on ontogenetic changes in the form and function of larval fish (e.g. Muller and Videler, 1996; Webb and Weihs, 1986), it remains unclear whether Weihs' (1980) theory, which is founded on measurements of force on rigid physical models, accurately characterizes the forces that act on an undulating body (Fuiman and Batty, 1997).

The present study used a combination of empirical measurements and mathematical modeling of the larvae of the ascidian *Botrylloides* sp. to test whether the hydrodynamics of swimming in these animals is better characterized by a quasi-steady or an unsteady model. By taking into account the acceleration reaction, skin friction and form force generated during swimming, models were used to formulate predictions in terms of the speed of freely swimming larvae and force generation. By comparing these predictions with measurements of force and speed, we were able to determine whether larvae generate thrust and drag by acceleration reaction (the unsteady model) or strictly by form force and skin friction (the quasi-steady model). Ascidians are an ideal group for exploring these hydrodynamics because the larvae of different species span nearly two orders of magnitude in *Re* [e.g. $\approx 5\times10^0$ in *Ciona intestinalis* (Bone, 1992); $Re \approx 10^2$ in *Distaplia occidentalis* (McHenry, 2001)].

Materials and methods

Colonies of *Botrylloides* sp. were collected in the months of August and September from floating docks (Spud Point Marina, Bodega Bay, CA, USA) in water that was between 14°C and 17°C. Colonies were transported in coolers and placed in a recirculating seawater tank at 16°C within 2 h of collection. To stimulate release of larvae, colonies were exposed to bright incandescent light after being kept in darkness overnight (Cloney, 1987). Released larvae were used in either force measurement experiments, free-swimming experiments or for morphometric analysis. In all cases, observation tanks were equipped with a separate outer chamber into which chilled water flowed from a water bath equipped with a thermostat (1166, VWR Scientific) that kept larvae at 16°C.

Force measurements

Larvae were individually attached to a calibrated glass micropipette tether in order to measure the forces that they generated during swimming. Each larva was held at the tip of the tether using light suction (Fig. 1) from a modified mouth pipette. This micropipette was anchored at its base with a rubber stopper that provided a flexible pivot. No bending in the micropipette was visible under a dissecting microscope when loaded at the tip of the tether. We therefore assumed that the micropipette was rigid and that deflections at the tip were due entirely to flexion at the pivot. The small deflections by the tether were recorded during calibration and larval swimming by a high-speed video camera (Redlake Imaging PCI Mono/1000S Motionscope, 156 pixels×320 pixels, 1000 frames s^{-1}) mounted on a compound microscope (Olympus, CHA), which was placed on its side at a right angle to the micropipette (Fig. 1). Video recordings of tether deflections made at the objective of the compound microscope were translated into radial deflections at the pivot of the micropipette (φ) using the following trigonometric relationship:

$$\varphi = \arctan\left(\frac{\delta}{h_{\text{objective}}}\right), \quad (1)$$

where δ is the linear deflection (away from its resting position) of the tether measured at the objective, and $h_{\text{objective}}$ is the distance from the tether pivot to the objective (Fig. 1A). In order to avoid changing the mechanical properties of the tether, room temperature was held at 22.2°C throughout experiments.

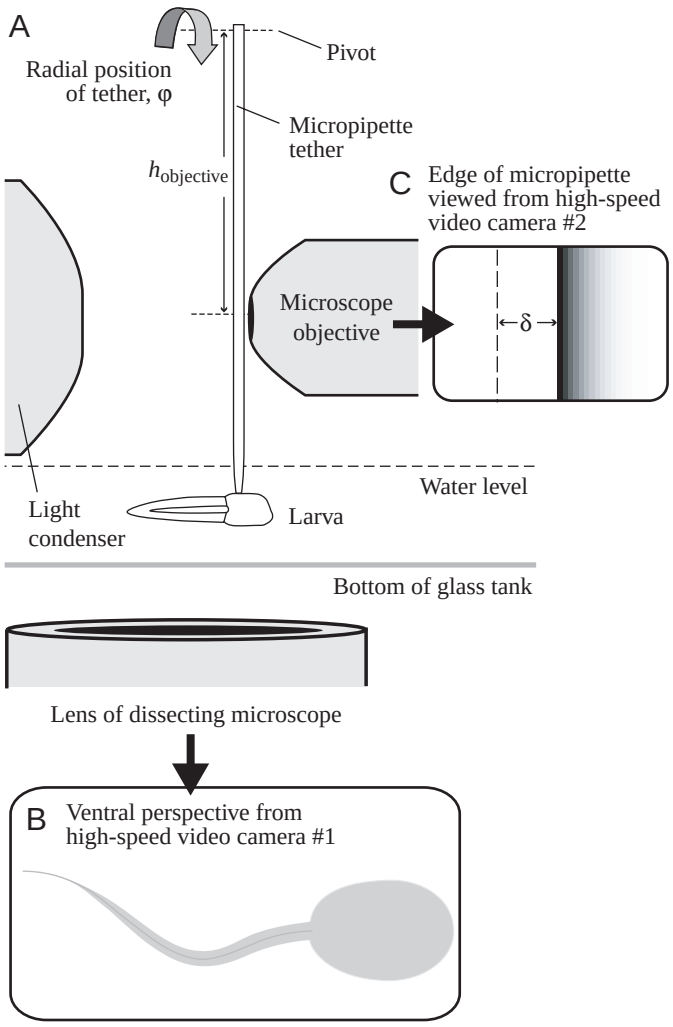

Fig. 1. The experimental set-up for tethering experiments. (A) We recorded the tail motion of a larva and the deflections of the tether to which a larva was attached. The larva is illustrated with the orientation that allowed for the recording of lateral forces: the longitudinal axis of the body is perpendicular to the direction of deflections. To measure thrust, the longitudinal axis was aligned parallel to the deflections of the tether. (B) The ventral perspective of a larva was recorded with video camera #1 mounted to a dissecting microscope mounted beneath the glass tank. (C) Deflections of the glass tether (δ) were recorded by video camera #2 mounted to a compound microscope.

The tether was modeled as a pendulum, with input force generated by the tail of a swimming larva (**F**) at the end and a damped spring at the pivot (Fig. 2). According to this model, the moments acting at the pivot were described by the following equation of motion (based on the equation for a damped pendulum; Meriam and Kraige, 1997a):

$$I_{tether}\frac{d^2\varphi}{dt^2} + k_{damp}\frac{d\varphi}{dt} + k_{spring}\varphi + (m_{tether}h_{cm} + m_{body}h_{tip})\boldsymbol{g}\sin(\varphi) + \mathbf{F}h_{tip} = 0\,, \quad (2)$$

where t is time, k_{damp} and k_{spring} are the damping coefficient (with units of Nms rad^{-1}) and spring coefficient (with units of Nm rad^{-1}), respectively, I_{tether} is the moment of inertia of the tether, m_{tether} and m_{body} are the mass of the tether and the body of the larva, respectively, $\boldsymbol{g}$ is the acceleration due to gravity, h_{cm} is the distance from the pivot to the center of mass of the tether, and h_{tip} is the distance from the pivot to the tip of the pipette. I_{tether} was calculated using the standard equation for a hollow cylinder (Meriam and Kraige, 1997a):

$$I_{tether} = \frac{1}{2}m_{tether}r_{tether}^2 + \frac{1}{12}m_{tether}h_{tip}^2\,, \quad (3)$$

where r_{tether} is the inner radius of the micropipette. We calculated the force generated by tethered larvae by solving equation 2 for **F**, using the measurements of tether deflections. We found that adding second- and third-order terms to equation 2 had a negligible effect (<0.5% difference) on force measurements. This suggests that any variation in stiffness or damping with strain or strain rate did not influence our measurements.

To calibrate the tether, we measured its stiffness and damping constants in a dynamic mechanical test. This test consisted of pulling and releasing the tether and then recording its passive movement over time (Fig. 2A). The tether oscillated like an underdamped pendulum (Meriam and Kraige, 1997a) with a natural frequency (101 Hz) well outside the range of tail-beat frequencies expected for ascidian larvae (McHenry, 2001). Using the equation of motion for the tether (equation 2, with **F**=0), its oscillations were predictable if the mass and the stiffness and damping coefficients were known. Conversely, we solved for the stiffness and damping coefficients from recordings of position and a measurement of the mass of the tether (see Appendix for details).

We examined how errors in our measurement of stiffness and damping coefficients were predicted to affect calculations of the force generated by larvae (Fig. 2C–H). By simulating the input force generated by a larva as a sine wave with an amplitude of 20 μN, we numerically solved equation 2 (using MATLAB, version 6.0, Mathworks) for the position of the tether over time at 1000 Hz (the sampling rate of our recordings). From these simulated recordings of tether position, we then solved equation 2 for **F**, the force generated by the larva. This circular series of calculations demonstrated that our sampling rate was sufficient to follow rapid changes in input force (Fig. 2C). Furthermore, we found that a minimum of 92% of the instantaneous moments resisting the input force were generated by the stiffness of the tether (i.e. the weight and damping of the tether provided a maximal 8% of the resistance to input force). If the values of stiffness and damping coefficients used in force measurements differed from those used to simulate tether deflections, then measured force did not accurately reflect the timing or magnitude of simulated force (Fig. 2D). This situation is comparable with using inaccurate values of stiffness and damping coefficients for measurements of force in an experiment.

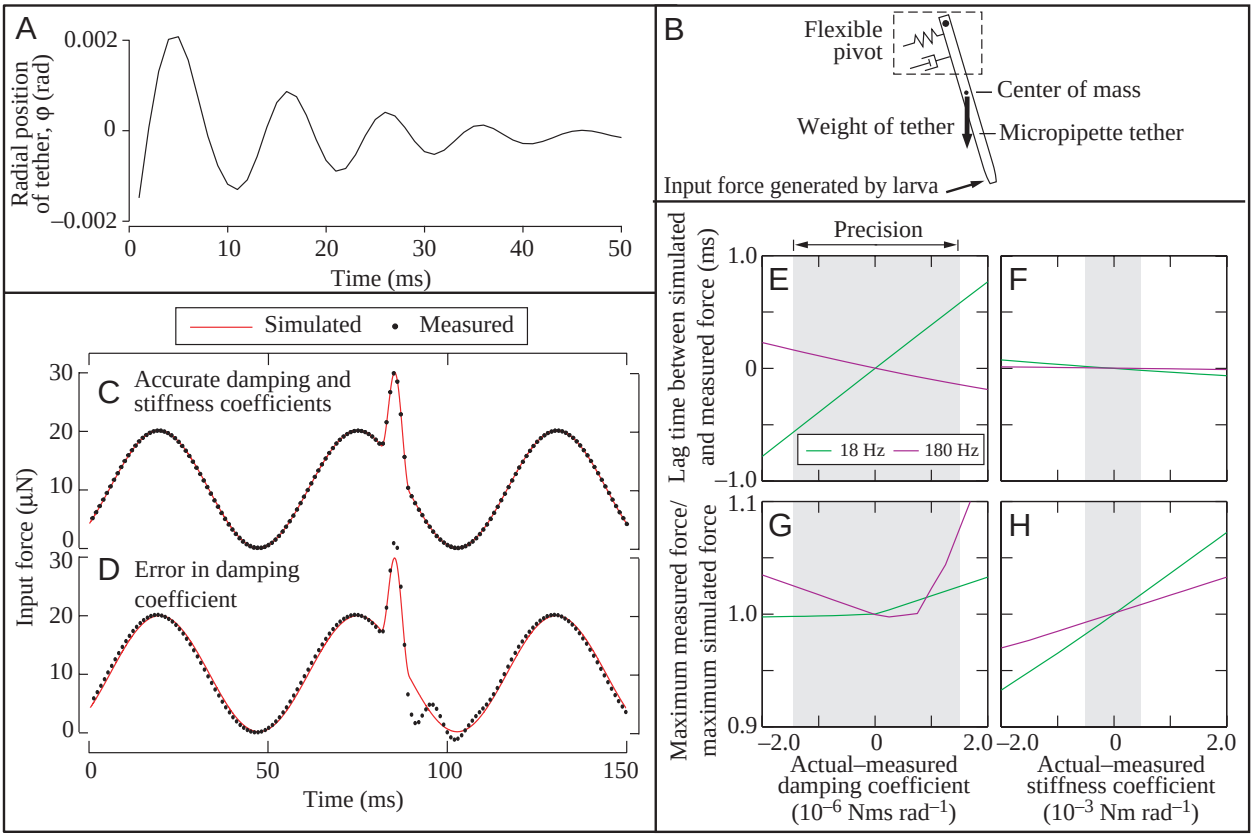

Fig. 2. The precision and accuracy of force measurements. (A) An example of the measurements of the passive movement of the tether after being pulled and released. These data were used to measure the coefficients of stiffness and damping (see Materials and methods). (B) A free-body diagram illustrates the forces acting on the tether during an experiment. The input force generated by a swimming larva is resisted by a component of the weight of the tether and the stiffness (illustrated by the spring) and damping of the pivot (illustrated by the dashpot). (C,D) Measurements of input force (filled circles) at 1000 Hz from the deflections of a tether (not shown) calculated from the simulated changes in force (red lines). (C) The input force measured from deflection measurements using accurate values for the stiffness and damping coefficients. (D) The input force measured using a damping coefficient that is less than the actual value (by 2×10^{-6} Nms rad^{-1}). (E,F) The time lag between simulated and measured input force for varying degrees of error in the damping (E) and stiffness (F) coefficients. (G,H) The ratio of maximum measured to maximum simulated input force for varying degrees of error in the damping (G) and stiffness (H) coefficients.

By varying the difference between the stiffness and damping coefficients used to simulate changes in tether position over time (i.e. the actual coefficients) and those used for force measurements (i.e. the measured coefficients), we explored how inaccuracy in measured coefficients was predicted to alter the timing and magnitude of measured force (Fig. 2E–H). We simulated changes in force at 18 Hz, to mimic oscillations in force at the tail-beat frequency (McHenry, 2001), and at 180 Hz, to simulate rapid changes in force. Within the level of precision (i.e. ±2 S.D.) of our measurements of stiffness and damping coefficients, measured force was not predicted to precede or lag behind simulated force by more than 1 ms, which is just 1.8% of an 18 Hz tail-beat period (Fig. 2E,F). Error in the damping coefficient may have caused measurements to overestimate rapidly changing force by as much as 7.5% (Fig. 2G). Within the precision of measured stiffness coefficients, measured forces may have differed from actual values by as much as 2.0% (Fig. 2H). These findings suggest that our measurements accurately reflect the timing of force generated by larvae, but the magnitude of force may be inaccurate by as much as 7.5%.

Midline kinematics

The ventral surface of the body was recorded during tethered swimming (Fig. 1A) with a high-speed video camera (Redlake Imaging PCI Mono/1000S Motionscope, 320 pixels×280 pixels, 500 frames s^{-1}) mounted to a dissecting microscope (Wild, M5A) beneath the glass tank containing the tethered larva. The video signal from this camera was recorded by the same computer (Dell Precision 410, with Motionscope 2.14 software, Redlake Imaging) as was used to record micropipette deflections, which allowed the recordings to be synchronized.

Coordinates describing the shape of the midline of the tail were acquired from video recordings, and the motion of the tail of larvae of *Botrylloides* sp. was characterized using the methodology presented by McHenry (2001). A macro program (on an Apple PowerMac G3 with NIH Image, version 1.62)

found 20 midline coordinates that were evenly distributed along its length (see McHenry, 2001 for details). In order to use the measured kinematics in our hydrodynamic models at any body length, we normalized all kinematic parameters to the body length of larvae (L, the distance from the anterior to posterior margins of the body) and the tail-beat period of their swimming (P; note that asterisks are used to denote non-dimensionality). According to McHenry (2001), the following equations describe the temporal variation in the change in the position of the inflection point along the length of the tail (z^*), the curvature of the tail between inflection points (κ^*), and the trunk angle (θ, the angle between the longitudinal axis of the trunk and the third midline coordinate, located at 0.15 tail lengths posterior to the intersection point of the trunk and tail):

$$z^*(t^*) = \varepsilon^* t^* , \tag{4}$$

$$\kappa^* = \frac{\alpha^*}{2}\left(-\cos\left(2\pi\,\frac{t^*}{\gamma^*}\right)+1\right), \tag{5}$$

$$\theta = \chi\sin(2\pi t^*), \tag{6}$$

where t^* is non-dimensional time, ε^* is the wave speed of inflection point, α^* is the amplitude of changes in curvature, γ^* is the period of change in curvature, and χ is the amplitude of change in trunk angle. Propagation initiates at the base of the tail after a phase lag of ζ^* from the time when the trunk angle passes through a position of zero.

Morphology and mechanics of the body

We measured the shape of the body to provide parameter values for our calculations of fluid forces and to estimate the body mass, center of mass and its moment of inertia. The peripheral shape of the body was measured (with NIH Image version 1.62 on an Apple PowerMac G3) using digital still images of larvae from dorsal and lateral views that were captured on computer (7100/80 PowerPC Macintosh with Rasterops 24XLTV frame grabber) using a video camera (Sony, DXC-151A) mounted on a dissecting microscope (Nikon, SMZ-10A). These images had a spatial resolution of 640 pixels×480 pixels, with each pixel representing approximately a 6 μm square with an 8-bit grayscale intensity value. Coordinates along the peripheral shape of the body were isolated by thresholding the image (i.e. converting from grayscale to binary; Russ, 1999). We found coordinates at 50 points evenly spaced along the length of the trunk and 50 points evenly spaced along the length of the tail (using MATLAB). From images of the lateral view, we used the same method to measure the dorso-ventral margins of the trunk, cellular tail and tail element. By the same method, we measured the width of the trunk from the dorsal view.

By assuming that the trunk was elliptical in cross-section and that the cellular region of the tail was circular in cross-section, we calculated the body mass, center of mass and moment of inertia using a program written in MATLAB from reconstructions of the body's volume. These calculations divided the volume of the body into small volumetric elements (each having a volume of Δw_i, where i is the element number) with the position of each element's center located at x_i and y_i coordinates with respect to the body's coordinate system. This system has its origin at the intersection between the trunk and tail, its x-axis running through the anterior-most point on the trunk, and its orthogonal y-axis oriented to the left of the body, on the frontal plane (as in McHenry, 2001). The tail fin was assumed to be rectangular in cross-section, with a thickness of 0.002 body lengths (measured from camera lucida drawings of tail cross-sections; Grave, 1934; Grave and Woodbridge, 1924). The mass of the body was calculated as the product of the tissue density (ρ_{body}) and the sum of volumetric elements that comprise the body:

$$m_{body} = \rho_{body}\sum_{i=1}^{q}\Delta w_i , \tag{7}$$

where q is the total number of volumetric elements. The position of the center of mass (**B**) was calculated as (Meriam and Kraige, 1997a):

$$\mathbf{B} = \frac{\rho_{body}}{m_{body}}\sum_{i=1}^{q}\Delta w_i\begin{bmatrix} x_i \\ y_i \end{bmatrix}. \tag{8}$$

The moment of inertia for the body about any arbitrary axis of rotation was described by the inertia tensor (**I**), calculated with the following equation (Meriam and Kraige, 1997a):

$$\mathbf{I} = \rho_{body}\sum_{i=1}^{q}\Delta w_i\begin{bmatrix} x_i^2 & -x_iy_i \\ -x_iy_i & y_i^2 \end{bmatrix}. \tag{9}$$

We calculated the forces generated by accelerating the mass of the tail in tethered swimming. This tail inertia force ($\mathbf{F}_{inertia}$) was calculated with the following equation:

$$\mathbf{F}_{inertia} = \rho_{body}\sum_{i=1}^{q}\Delta w_i\,\frac{d\mathbf{V}_i}{dt} , \tag{10}$$

where $\mathbf{V}_i$ is the velocity of the tail element. In order to remove from the measurements any force not generated by fluid forces, we subtracted the tail inertia force from the measured force in our comparisons with predicted forces.

In order to test the effect of tissue density, we ran simulations (see 'Modeling free swimming' below) with the mean kinematics and morphometrics at high tissue density (ρ_{body}=1.250 g ml^{-1}, the density of an echinopluteus larva of an echinoid with calcareous spicules; Pennington and Emlet, 1986) and low tissue density (ρ_{body}=1.024 g ml^{-1}, the density of seawater at 20°C; Vogel, 1981). All other simulations were run with a tissue density typical of marine invertebrate larvae not possessing a rigid skeleton (ρ_{body}=1.100 g ml^{-1}; Pennington and Emlet, 1986).

Kinematics of freely swimming larvae

Freely swimming larvae were filmed simultaneously with two digital high-speed video cameras (recording at 500 frames s^{-1})

using the methodology described by McHenry and Strother (in press). These cameras (Redlake PCI Mono/100S Motionscope, 320 pixels×280 pixels per camera, each equipped with a 50 mm macro lens, Sigma) were directed orthogonally and both were focused on a small volume (1 cm^3) of water in the center of an aquarium (with inner dimensions of 3 cm width × 3 cm depth × 6 cm height). Larvae were illuminated from the side with two fiberoptic lamps (Cole Parmer 9741-50).

We recorded the swimming speed of larvae by tracking, in three dimensions, the movement of the intersection between the trunk and tail during swimming sequences. From the mean values of swimming speed ($\bar{u}$), we calculated a *Re* of the body for freely swimming larvae using the following equation:

$$Re = \frac{\rho L \bar{u}}{\mu} . \quad (11)$$

Hydrodynamic forces and moments generated by the tail

We modeled the hydrodynamics of the tail using a blade-element approach that divided the length of the tail into 50 tail elements and calculated the force generated by each of these elements. Each element was dorso-ventrally oriented, meaning that the length of each element ran from the dorsal to the ventral margins of the fin. For each instant of time in a swimming sequence, the force acting on each element ($\mathbf{E}_j$, where j is the tail element number) was calculated by assuming that it generated the same force as a comparably sized flat plate moving with the same kinematics. Our models assume that each tail element generates force that is independent of neighboring elements. This neglects any influence that flow generated along the length of the body may have on force generation. The total force generated by such a plate is the sum of as many as three forces: the acceleration reaction ($\mathbf{E}_{ja}$), skin friction ($\mathbf{E}_{js}$) and the form force ($\mathbf{E}_{jf}$; Fig. 3). The contribution of each of these forces to the total force and moment instantaneously generated by the tail was calculated by taking the sum of forces and moments generated by all elements (see Appendix). Dividing the tail into 75 and 100 tail elements did not generate predictions of forces or moments that were noticeably different from predictions generated with 50 tail elements, but models with 25 tail elements did generate predictions different from models with 50 elements. Therefore, we ran all simulations with 50 tail elements.

We modeled the swimming of larvae with both quasi-steady and unsteady models. In the quasi-steady model, the force generated by the tail ($\mathbf{F}$) was calculated as the sum of skin friction ($\mathbf{F}_s$) and the form force ($\mathbf{F}_f$; $\mathbf{F}=\mathbf{F}_f+\mathbf{F}_s$), and the total moment ($\mathbf{M}$) was calculated as the sum of moments generated by skin friction ($\mathbf{M}_s$) and the form force ($\mathbf{M}_f$; $\mathbf{M}=\mathbf{M}_f+\mathbf{M}_s$). According to this model, the force acting on a tail element is equal to the sum of the form force and skin friction acting on the element ($\mathbf{E}_j=\mathbf{E}_{jf}+\mathbf{E}_{js}$; Fig. 3B). In the unsteady model, the force generated by the tail was calculated as the sum of all three forces ($\mathbf{F}=\mathbf{F}_f+\mathbf{F}_s+\mathbf{F}_a$, where $\mathbf{F}_a$ is the acceleration reaction generated by the tail), and the total moment was calculated as the sum of moments generated by all three forces

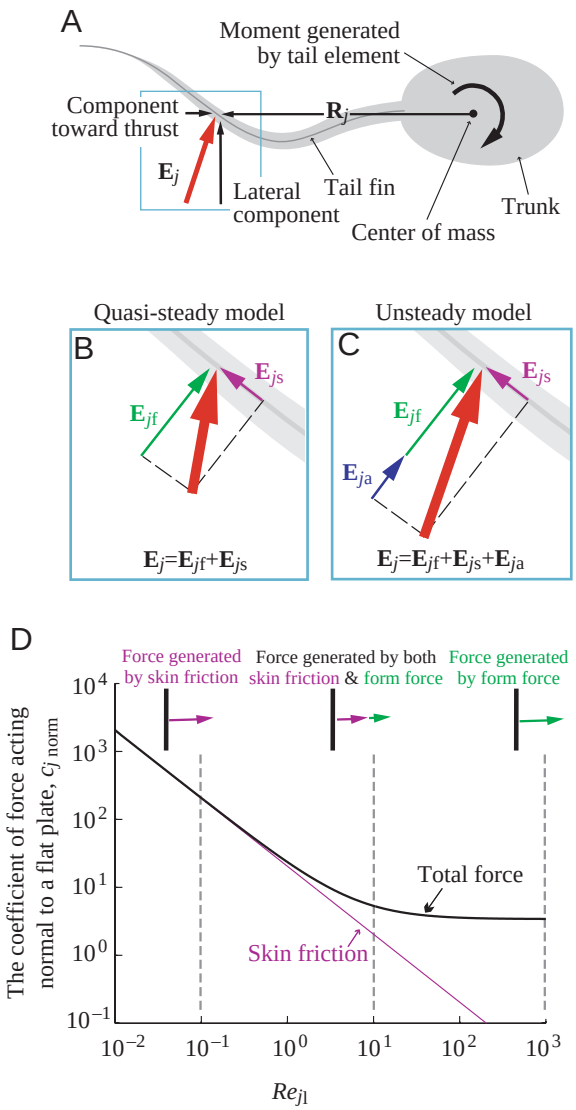

Fig. 3. Schematic drawing of the quasi-steady and unsteady hydrodynamic models. (A) The force generated by a single tail element ($\mathbf{E}_j$) is drawn on the silhouette of the body of a larva from a dorsal perspective. The force generated by this element has components acting towards thrust and laterally. The force generated by the whole tail was calculated instantaneously as the sum of force generated by all tail elements. The position vector of the element ($\mathbf{R}_j$) with respect to the center of mass describes the lever arm used by the tail element to generate a moment about the center of mass. (B,C) Each of the models is illustrated by the vectors that comprise the force generated by the tail element. (B) The force acting on tail elements ($\mathbf{E}_j$) in the quasi-steady model was calculated as the sum of the form force ($\mathbf{E}_{jf}$) and skin friction ($\mathbf{E}_{js}$). (C) The force acting on tail elements in the unsteady model was the sum of the quasi-steady forces and the acceleration reaction ($\mathbf{E}_{ja}$). (D) The coefficient of force acting normal to the surface of a flat plate ($c_{j\,norm}$) oriented normal to flow. The form force (in green; see equation 21) is found as the difference between the total force (in black; see equation 18) and the force generated by skin friction (in violet; see equation 19). The total force is generated primarily by form force at height-specific Reynolds numbers (Re_{jl}) of ≈10^3, skin friction is dominant at $Re_{jl}<10^0$, but the normal force is a combination of the two at intermediate *Re* values.

($\mathbf{M}=\mathbf{M}_f+\mathbf{M}_s+\mathbf{M}_a$, where $\mathbf{M}_a$ is the moment generated by the acceleration reaction). According to the unsteady model, the force acting on a tail element is equal to the sum of the form force, skin friction and acceleration reaction ($\mathbf{E}_j=\mathbf{E}_{jf}+\mathbf{E}_{js}+\mathbf{E}_{ja}$; Fig. 3C).

The acceleration reaction

The acceleration reaction generated by a tail element was calculated as the product of the added mass coefficient (c_{ja}), the density of water (ρ) and the component of the rate of change in the velocity of the element that acts in the direction normal to the element's surface and lies on the frontal plane of the body ($\mathbf{V}_{j\,\mathrm{norm}}$; Lighthill, 1975):

$$\mathbf{E}_{ja} = -c_{ja}\rho \frac{\mathrm{d}\mathbf{V}_{j\,\mathrm{norm}}}{\mathrm{d}t} . \quad (12)$$

The added mass coefficient was estimated as (Lighthill, 1975):

$$c_{ja} = \frac{1}{4}\pi l_j^2 \Delta s , \quad (13)$$

where l_j is the distance between dorsal and ventral margins of the fin (height of a tail element), and Δs is the width of the tail element. Note that this is the added mass coefficient for inviscid flow and is assumed not to vary with *Re*.

Skin friction

At $Re<10^2$, skin friction may generate force that is both normal and tangent to a surface. Therefore, the equation for skin friction on a tail element combines analytical approximations for skin friction acting tangent (Schlichting, 1979) and normal (Hoerner, 1965) to the surface of a flat plate:

$$\mathbf{E}_{js} = -\left(\frac{32}{\pi}\mathbf{V}_{j\,\mathrm{norm}} + 0.32\frac{l_j}{s_j}\sqrt{Re_{js}}\mathbf{V}_{j\,\mathrm{tan}}\right)\mu\Delta s , \quad (14)$$

where $\mathbf{V}_{j\,\mathrm{tan}}$ is the tangent component of the velocity of the element, s is the distance along the tail from the tail base to the element, and Re_{js} is the position-specific Reynolds number for a tail element. This Reynolds number was calculated as:

$$Re_{js} = \frac{\rho s_j \bar{v}_j}{\mu} , \quad (15)$$

where s_j is the position of the element down the length of the tail, $\bar{v}_j$ is the time-averaged value for tail element speed over the tail-beat cycle.

Form force

The form force acts normal to a surface and varies with the square of flow speed, as expressed by the following equation (Batchelor, 1967):

$$\mathbf{E}_{jf} = -\frac{1}{2}\rho l_j c_{jf} v_{j\,\mathrm{norm}}\mathbf{V}_{j\,\mathrm{norm}}\Delta s , \quad (16)$$

where $v_{j\,\mathrm{norm}}$ is the magnitude (or speed) of the normal component of the velocity of the tail element, and c_{jf} is the force coefficient for the form force. At $Re\geq10^2$, the force acting normal to the surface of a plate is dominated by the form force (Granger, 1995; Sane and Dickinson, 2002), so c_{jf} may be considered equivalent to the coefficient of force measured normal to the surface of the plate, $c_{j\,\mathrm{norm}}$. This coefficient may be calculated from measurements of force on a flat plate with the following equation:

$$c_{j\,\mathrm{norm}} = \frac{2\mathbf{F}_{\mathrm{norm}}}{\rho l_j v_{j\,\mathrm{norm}}\mathbf{V}_{j\,\mathrm{norm}}\Delta s} \quad (17)$$

where $\mathbf{F}_{\mathrm{norm}}$ is the force measured on the plate in the normal direction, $c_{j\,\mathrm{norm}}=3.42$ is an appropriate approximation for tail elements at high *Re* (Dickinson et al., 1999).

The contribution of the form force to the total force acting on a flat plate is predicted to change with *Re* (Fig. 3D). Using the form of the curve-fit equation for changes in the force coefficient on a sphere at different *Re* given by White (1991), the following equation gives the force coefficient generated by both form force and skin friction ($c_{j\,\mathrm{s+f\,norm}}$) over intermediate *Re* ($10^0<Re<10^3$):

$$c_{j\,\mathrm{s+f\,norm}} = 3.42 - \frac{1}{1+\sqrt{Re_{jl}}} + \frac{64}{\pi Re_{jl}} , \quad (18)$$

where Re_{jl} is the height-specific Reynolds number of the tail element (described below). The first and last terms in this equation describe the force generated at high ($Re_{jl}<10^2$) and low ($Re_{jl}<10^0$) Reynolds numbers, respectively, and the second term is an intermediary fit to the experimental data reviewed by Hoerner (1965). In the viscous regime ($Re_{jl}<10^0$), skin friction dominates the force acting on a plate. The force coefficient in the normal direction for a tail element generated entirely by skin friction is given by the following equation (Lamb, 1945):

$$c_{js\,\mathrm{norm}} = \frac{64}{\pi Re_{jl}} . \quad (19)$$

The height-specific Reynolds number of a tail element was calculated as:

$$Re_{jl} = \frac{\rho l_j \bar{v}_j}{\mu} . \quad (20)$$

Subtracting the contribution of skin friction (equation 19) from the coefficient for the total normal force (equation 18) yields the coefficient for the form force for a tail element:

$$c_{jf} = 3.42 - \frac{1}{1+\sqrt{Re_{jl}}} . \quad (21)$$

Hydrodynamic forces and moments generated by the trunk

The force acting on the trunk ($\mathbf{T}$) was assumed to be the same as that acting on a sphere with the same kinematics and a diameter equal to the length of the trunk. At intermediate *Re*, this force is equal to the sum of skin friction ($\mathbf{T}_s$) and the form

force ($\mathbf{T}_f$). The form force varies with the square of the velocity of the trunk (**P**; Batchelor, 1967):

$$\mathbf{T}_f = -\frac{1}{2}\rho S k_f p \mathbf{P}\,, \tag{22}$$

where ρ is the density of water, S is the projected area of the trunk, p is the speed of the trunk and k_f is the coefficient of the form force on a sphere, which varies with Re in the following way (with skin friction subtracted; White, 1991):

$$k_f = \frac{6}{1+\sqrt{Re_a}} + 0.4\,, \tag{23}$$

where Re_a is the Reynolds number of the trunk (calculated using equation 11 with the length of the trunk, a, used as the characteristic length). The skin friction acting on a sphere is predicted by Stokes law (Batchelor, 1967):

$$\mathbf{T}_s = 3\pi a \mu \mathbf{P}\,. \tag{24}$$

Given the relatively low value for the added mass coefficient of a sphere (0.5) and the low accelerations expected by the trunk during steady swimming, we assumed negligible force generation by the acceleration reaction acting on the trunk. The trunk generated a moment (**O**) about the center of mass, which was the sum of moments generated by the form force and skin friction acting on the trunk:

$$\mathbf{O} = \mathbf{D} \times \mathbf{T}_f + \mathbf{D} \times \mathbf{T}_s\,, \tag{25}$$

where **D** is the position vector for the center of volume of the trunk with respect to the body's center of mass.

Modeling free swimming

Using the equations that describe the hydrodynamics of swimming, we modeled the dynamics of free swimming to calculate predicted movement by the center of mass of a swimming ascidian larva. The acceleration of the body (**A**) was calculated as the sum of hydrodynamic forces acting on the body, divided by body mass:

$$\mathbf{A} = \frac{\mathbf{F}+\mathbf{T}}{m_{body}}\,. \tag{26}$$

The angular acceleration about the center of mass was calculated using the following equation (based on Symon, 1960):

$$\frac{d\boldsymbol{\Omega}}{dt} = \mathbf{I}^{-1}\left((\mathbf{M}+\mathbf{O}) - \boldsymbol{\Omega}(\mathbf{I}^B \cdot \boldsymbol{\Omega}) - \frac{d\mathbf{I}^B}{dt}\cdot\boldsymbol{\Omega}\right), \tag{27}$$

where $\boldsymbol{\Omega}$ is the rate of rotation vector about the center of mass, and $\mathbf{I}^B$ is the inertia tensor given in the body's coordinate system (with the center of mass as its origin). The velocity and position of the body's center of mass were calculated in two dimensions from the respective first and second time integrals of equation 26, and the rate of rotation and orientation of the body were calculated from the respective first and second time integrals of equation 27. In order to calculate these integrals, models were programmed in MATLAB using a variable-order Adams–Bashforth–Moulton solver for integration (Shampine and Gordon, 1975). This is a non-stiff multistep solver, which means that it uses the solutions at a variable number of preceding time points to compute the current solution.

We calculated the percentage of thrust and drag generated by the form force and skin friction in order to evaluate the relative importance of these forces to propulsion. This percentage was calculated individually for the trunk and tail and for both thrust and drag. For example, the following equation was used to calculate the percentage of thrust generated by the form force on the tail ($H_{f\,tail}$):

$$H_{f\,tail} = \frac{\mathbf{F}'_f}{\mathbf{F}'_s + \mathbf{F}'_f + \mathbf{F}'_s + \mathbf{F}'_f} \times 100\%\,, \tag{28}$$

where $\mathbf{F}'_f$ and $\mathbf{F}'_s$ are the form force and skin friction, respectively, generated by the tail in the direction of thrust (i.e. towards the anterior of the trunk). Similar calculations were also made for the percentage of skin friction generated by the tail, form force generated by the trunk, and skin friction generated by the trunk.

In order to examine how the relative magnitude of form force and skin friction changes with the Re of the body, we ran a series of simulations using model larvae of different body lengths. Each simulation used the mean morphometrics and kinematic parameter values. The non-dimensional morphometrics and kinematics were scaled to the mean measured tail-beat period and the body length used in the simulation. This means that animations of the body movements in the model appeared identical for all simulations (i.e. models were kinematically and geometrically similar), despite being different sizes.

Statistical comparisons between measurements and predictions

We tested our mathematical models by comparing the measured forces and swimming speeds of larvae with model predictions. We measured the mean thrust (force directed towards the anterior) and lateral force generated by a tethered larva and used our model to predict those forces using the same kinematics as measured for the tethered larva and the mean body dimensions. Such measurements and model predictions were made for a number of larvae, and a paired Student's t-test (Sokal and Rohlf, 1995) was used to compare measured and predicted forces. Such comparisons were made with predictions from both the quasi-steady model and the unsteady model.

Predictions of mean swimming speeds from both models were compared with measurements of speed. Model predictions of swimming speed were generated using the mean body dimensions and the tail kinematics of individual larvae measured during tethered swimming. This assumes that the midline kinematics of freely swimming larvae were not dramatically different from that of tethered

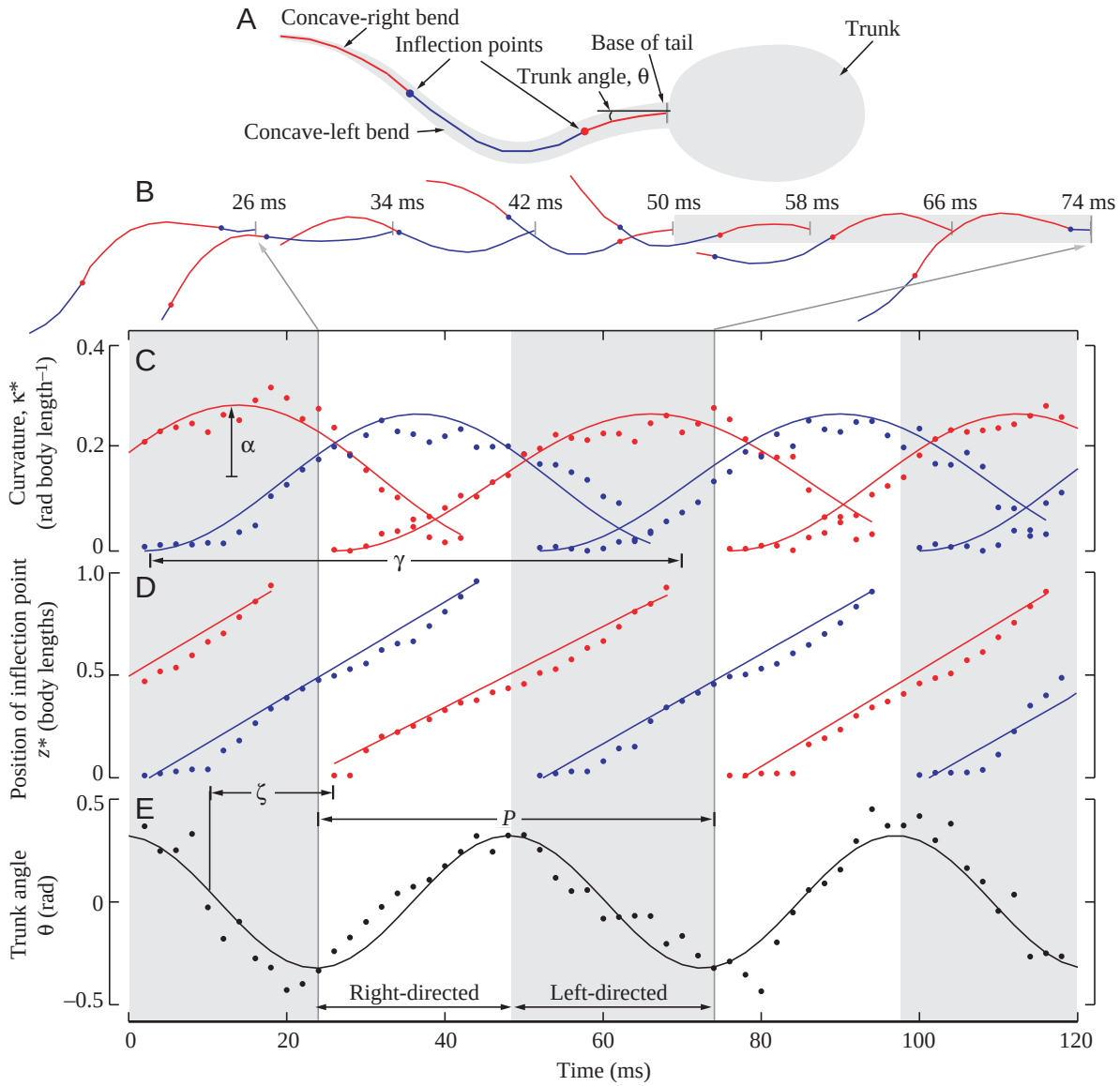

Fig. 4. The undulatory motion typical of tethered larvae. (A) The shape of the tail of a larva at any instant was described by the trunk angle (θ), position of inflection points on the tail (*z*) and the curvature of the tail between the inflection points (κ*). The trunk angle was positive when the tail was bent to the right and negative when bent to the left of the body. (B) Changes in the midline of the tail of a larva over a single tail beat. Notice that as time progresses (to the right), inflection points (filled circles) move down the midline in the posterior direction (away from the base of the tail). (C–E) Points represent measurements of each kinematic parameter and the curves are found by a least-squares fit to functions described in the Materials and methods. (C) The curvature of bends between inflection points (with a period γ) in both concave-left and concave-right bends (having an amplitude α). (D) The propagation of inflection points begins at the tail base with a phase lag of ζ with respect to a zero value of the trunk angle. (E) The trunk angle oscillates with time (with a period *P*). The vertical gray bands show when the trunk angle is directed towards the left side of the body, and white bands occur when the trunk angle is directed to the right.

larvae. Mean swimming speeds were measured on a different sample of freely swimming larvae, and an unpaired *t*-test (Sokal and Rohlf, 1995) was used to compare predictions of swimming speed with measurements. We verified that samples did not violate the assumption of a normal distribution by testing samples with a Kolomogorov–Smirnov test (samples with $P>0.05$ were considered to be normally distributed).

Results

Hydrodynamics at Re≈10^2

Tethered larvae

Using measured kinematics (Fig. 4, Table 1), we tested the ability of hydrodynamic models to predict both the timing and mean values of forces generated by larvae. The magnitude of predictions of form force and the acceleration reaction (Fig. 5A–C) were approximately two orders of magnitude

Table 1. *Swimming kinematics of tethered larvae*

Individual	L (mm)	P (ms)	ε^* (body lengths per tail-beat period)	α^* (rad per body length)	γ^* (tail-beat periods)	χ (rad)
1	1.91	41.7	1.18	0.77	1.25	0.08
2	1.93	44.5	1.13	0.87	1.11	0.28
3	2.07	41.0	1.14	1.16	1.29	0.20
4	1.93	41.8	1.27	1.06	1.18	0.27
5	2.10	50.0	1.13	1.13	1.04	0.32
6	1.90	47.6	1.39	0.99	1.19	0.16
7	1.76	41.8	1.17	0.81	1.25	0.16
8	1.72	43.6	1.26	0.93	1.03	0.34
9	1.90	39.4	1.10	1.07	1.04	0.28
10	1.71	40.2	1.30	0.94	1.37	0.28
11	2.07	41.8	1.12	1.04	1.40	0.14
12	1.85	40.2	1.47	0.84	1.26	0.11
13	2.02	41.8	1.03	0.86	1.22	0.16
14	2.09	42.7	1.31	1.07	1.37	0.16
Mean ± 1 S.D.=	1.93±0.13	42.7±2.9	1.21±0.12	0.97±0.12	1.21±0.12	0.21±0.08

L, body length; P, tail-beat period; ε, wave speed of inflection point; α, amplitude of tail curvature; γ, period of tail curvature; χ, amplitude of trunk angle.

All data are time-averaged values for the duration of at least three tail beats.

Table 2. *Model verification in tethered and freely-swimming larvae*

		Model predictions				
	Measurements	Quasi-steady ($\mathbf{F}=\mathbf{F}_f+\mathbf{F}_s$)	P	Unsteady ($\mathbf{F}=\mathbf{F}_f+\mathbf{F}_s+\mathbf{F}_a$)	P	N
Lateral force (μN)	5.11±2.31	4.09±1.59	0.181	4.74±1.45	0.600	11
Thrust (μN)	6.07±1.93	3.72±1.36	0.297	4.56±1.29	0.450	3
Swimming speed (mm s^{-1})	31.36±5.17	27.63±7.09	0.123	41.29±6.09	<0.001	14

All values are means ± 1 S.D. P values are the results of a Student's t-test that compared measurements with predictions. These were paired comparisions of force and unpaired comparisons of speed.

greater than the predictions for the tail inertia and skin friction forces (Fig. 5D,E). Due to the low magnitude of skin friction, the tail force predicted in the lateral direction by the quasi-steady model ($\mathbf{F}=\mathbf{F}_f+\mathbf{F}_s$) was qualitatively indistinguishable from the prediction of form force (Fig. 5F). The prediction for the tail force in the lateral direction by the unsteady model had the addition of the acceleration reaction ($\mathbf{F}=\mathbf{F}_f+\mathbf{F}_s+\mathbf{F}_a$), which generated peaks of force when the form force was low in magnitude (Fig. 5F). These force peaks were not reflected in the measurements of lateral force (Fig. 5G). This measured force oscillated in phase with trunk angle (θ; phase lag mean ± 1 S.D.=0.03±0.02 tail-beat periods, P=0.230, N=11; Figs 5H, 6), unlike the acceleration reaction, which was predicted to be out of phase with trunk angle. Both quasi-steady and unsteady models predicted mean thrust and mean lateral force that was statistically indistinguishable from measurements (Table 2).

The force predictions by the quasi-steady model more closely matched the timing of measurements than those of the unsteady model (Fig. 7). The force predicted by the quasi-steady model ($\mathbf{F}=\mathbf{F}_f+\mathbf{F}_s$) oscillated in phase with measured lateral forces. However, the unsteady model ($\mathbf{F}=\mathbf{F}_f+\mathbf{F}_s+\mathbf{F}_a$) predicted peaks of force generation by the acceleration reaction acting in the direction opposite to the measured force (Figs 5, 7). At instants of high tail speed, the form force was large and was followed by the acceleration reaction acting in the opposite direction as the tail decelerated and reversed direction. Although both models accurately predicted mean forces (Table 2), the timing of force production suggests that the acceleration reaction does not generate propulsive force in the swimming of ascidian larvae.

Freely swimming larvae

Simulations of free swimming allowed the body of larvae to rotate and translate in response to the hydrodynamic forces generated by the body. As such movement could contribute to the flow encountered by a swimming larva, the forces generated by freely swimming larvae were not assumed to be the same as those generated by tethered larvae. Therefore,

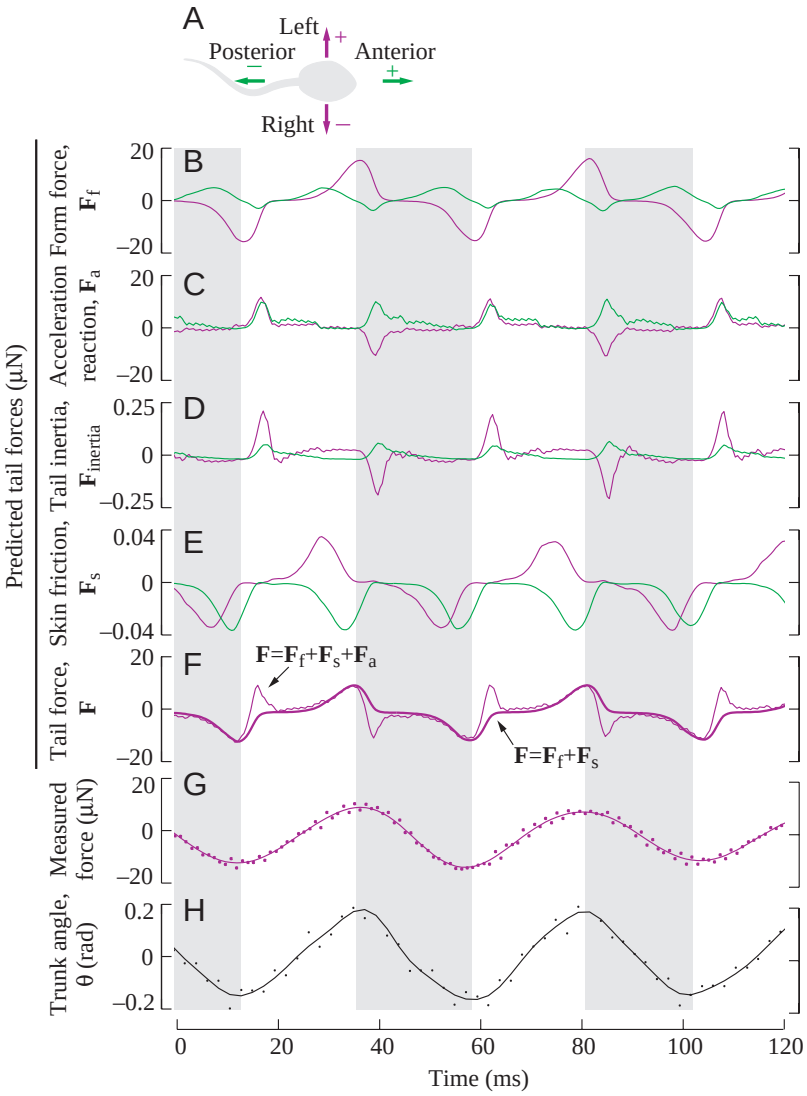

Fig. 5. Measured and predicted forces for a tethered larva. (A) The legend for the direction of force data (B–H). Violet traces represent lateral forces that are directed to the right of the body when negative and to the left when positive. Green traces show force along the antero-posterior axis of the trunk that is directed toward the anterior when positive and toward the posterior when negative. (B–H). As in Fig. 4, the vertical gray bands show when the trunk angle (θ) is directed toward the left side of the body, and white bands occur when the trunk angle is directed to the right. Note that (B) the form force and (C) the acceleration reaction are on the same scale as the measured force, but both (D) the tail inertia force and (E) skin friction are plotted on smaller scales. (F) The tail force predicted for quasi-steady ($\mathbf{F}=\mathbf{F}_f+\mathbf{F}_s$, heavy line) and unsteady models ($\mathbf{F}=\mathbf{F}_f+\mathbf{F}_s+\mathbf{F}_a$, thin line) illustrate the differences between these models. (G) Force generated by the larva against the tether, in the lateral direction for unfiltered (points) and filtered (line) data (see text for details). (H) Variation in trunk angle with time (the line is filtered data and the points are unfiltered).

simulations of free swimming were a closer approximation of the dynamics of freely swimming larvae and provided a test for whether the results of tethering experiments apply to freely swimming larvae.

The results of these simulations support the result from tethering experiments that the acceleration reaction does not play a role in the hydrodynamics of swimming. The quasi-steady model ($\mathbf{F}=\mathbf{F}_f+\mathbf{F}_s$) predicted a mean swimming speed that was statistically indistinguishable from measured mean swimming speed. By contrast, the unsteady model ($\mathbf{F}=\mathbf{F}_f+\mathbf{F}_s+\mathbf{F}_a$) predicted a mean swimming speed that was significantly different from measurements (Table 2). We found small (<4%) differences in predicted mean speed between models using a high ($\rho_{body}=1.250\,g\,ml^{-1}$) and low ($\rho_{body}=1.024\,g\,ml^{-1}$) tissue density, suggesting that any inaccuracy in the tissue density used for simulations ($\rho_{body}=1.100\,g\,ml^{-1}$) had a negligible effect on predictions.

Reynolds number values varied among different regions of the body (Table 3). The mean Reynolds number for the whole body ($Re=7.7\times10^1$) was larger than the Reynolds number for the trunk ($Re_a=2.8\times10^1$) because the whole body is greater in length than the length of just the trunk. The mean height-specific Reynolds number (Re_{jl}) and the mean position-specific Reynolds number (Re_{js}) were larger towards the posterior (Table 3).

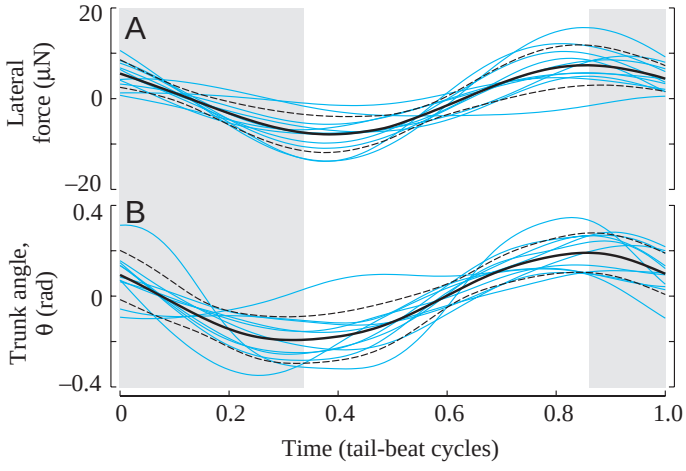

Fig. 6. The phase relationship between lateral force generation and tail kinematics. Positive values are directed to the left of the body and negative values are directed to the right. Each blue curve shows the mean values over four tail beats for a single larva, with time normalized to the tail-beat period. The black solid lines represent the mean, and the black dotted lines represent ±1 S.D. for all larvae (N=11). As in Fig. 4, the gray band shows when the trunk angle is directed towards the left side of the body, and white bands show when the trunk angle is directed to the right. Measurements of lateral force (A) are plotted above trunk angle (B).

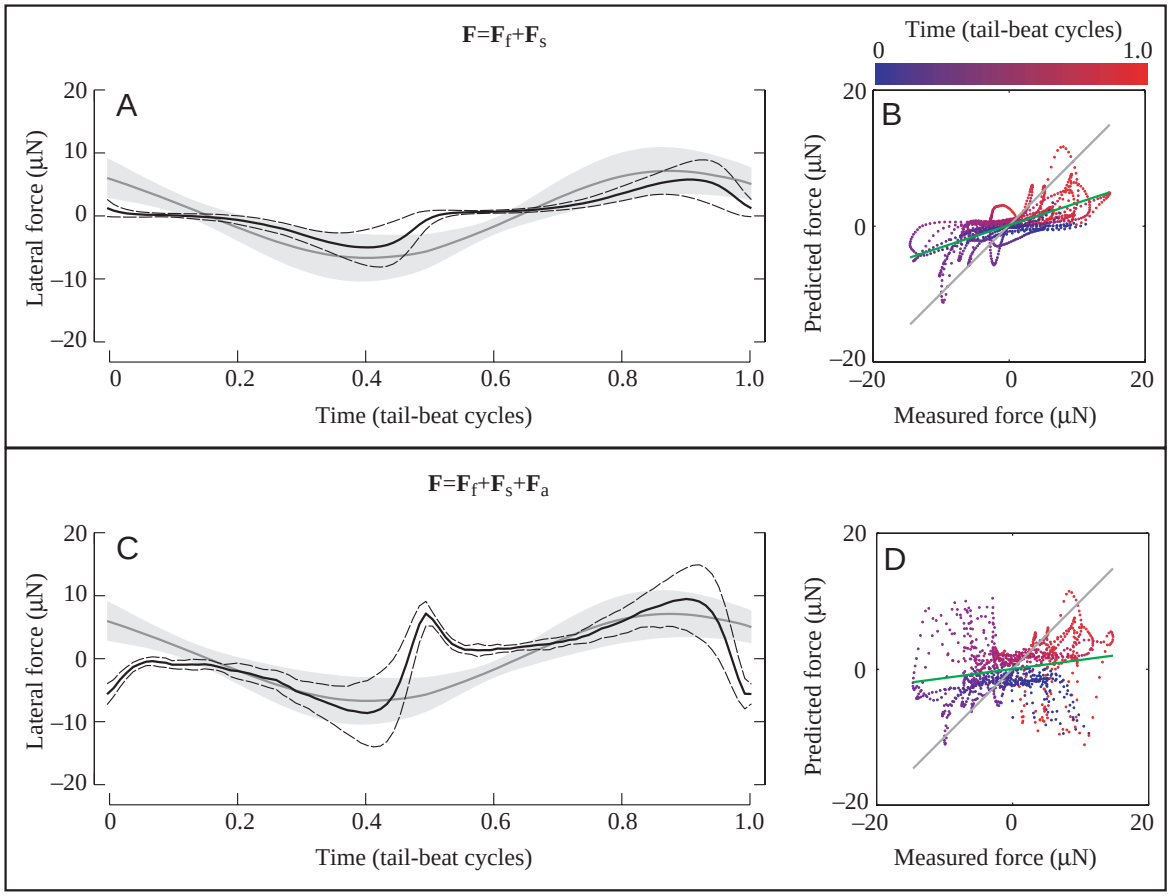

Fig. 7. Comparison of predicted and measured lateral forces. Graphs to the left (A and C) show mean measured lateral forces (dark gray line) ±1 S.D. (light gray fill) of measured forces (the same data as in Fig. 5A; N=11) and the mean (solid black line) ±1 S.D. (dotted black line) of predicted lateral forces for the same 11 larvae. Graphs on the right (B and D) present the same data, but the measured forces are plotted against predicted forces for each instant of time in the tail-beat cycle. Points vary in color from blue to red as the tail-beat cycle progresses. The green regression line was calculated by a least-squares solution to a linear curve fit of the data (slope=0.32, y-intercept=0, r^2=0.50 in B; slope=0.13, y-intercept=0, r^2=0.05 in D). The gray line has a slope of 1, which represents a perfect match between measured and predicted data. (A,B) The forces predicted for the lateral force by the quasi-steady model compared with measurements. (C,D) The forces predicted for the lateral force by the unsteady model compared with measurements.

Hydrodynamics at 10^0<Re<10^2

Predictions by the quasi-steady model showed how thrust and drag may be generated differently by form force and skin friction at different *Re*. At *Re*≈10^0, both thrust and drag were predicted to be dominated (>95%) by skin friction acting on the trunk and tail (Fig. 8A,B). At *Re*≈10^1, most drag (63%) was generated by skin friction acting on the trunk, and most thrust (69%) was generated by skin friction acting on the tail (Fig. 8C,D). At *Re*≈10^2, drag was generated by a combination of skin friction and form force, but thrust was generated almost entirely by form force acting on the tail (Fig. 8E,F). By running simulations throughout the intermediate *Re* range (10^0<*Re*<10^2), we found that form force gradually dominates thrust generation (up to 98%) with increasing *Re*. Although the proportion of drag generated by form force increases with *Re*, skin friction generates a greater proportion of drag (>62%) than does form force, even at *Re*≈10^2.

Discussion

The acceleration reaction

It is surprising that our results suggest that the acceleration reaction does not contribute to thrust and drag in the steady undulatory swimming of *Botrylloides* sp. larvae. Vyman's (1974) model for the energetics of steady swimming in fish larvae assumes that the acceleration reaction should operate at the Reynolds number at which these larvae swim (*Re*≈10^2). Although the energetic costs of locomotion predicted by Vyman (1974) show good agreement with measurements, these predictions from an unsteady model have not been compared with the predictions of a quasi-steady model. Furthermore, the hydrodynamics assumed by Vyman (1974) have yet to be experimentally tested. By contrast, Jordan (1992) did compare quasi-steady and unsteady predictions with measurements of the startle response behavior of the chaetognath *Sagitta elegans*. This study found that the

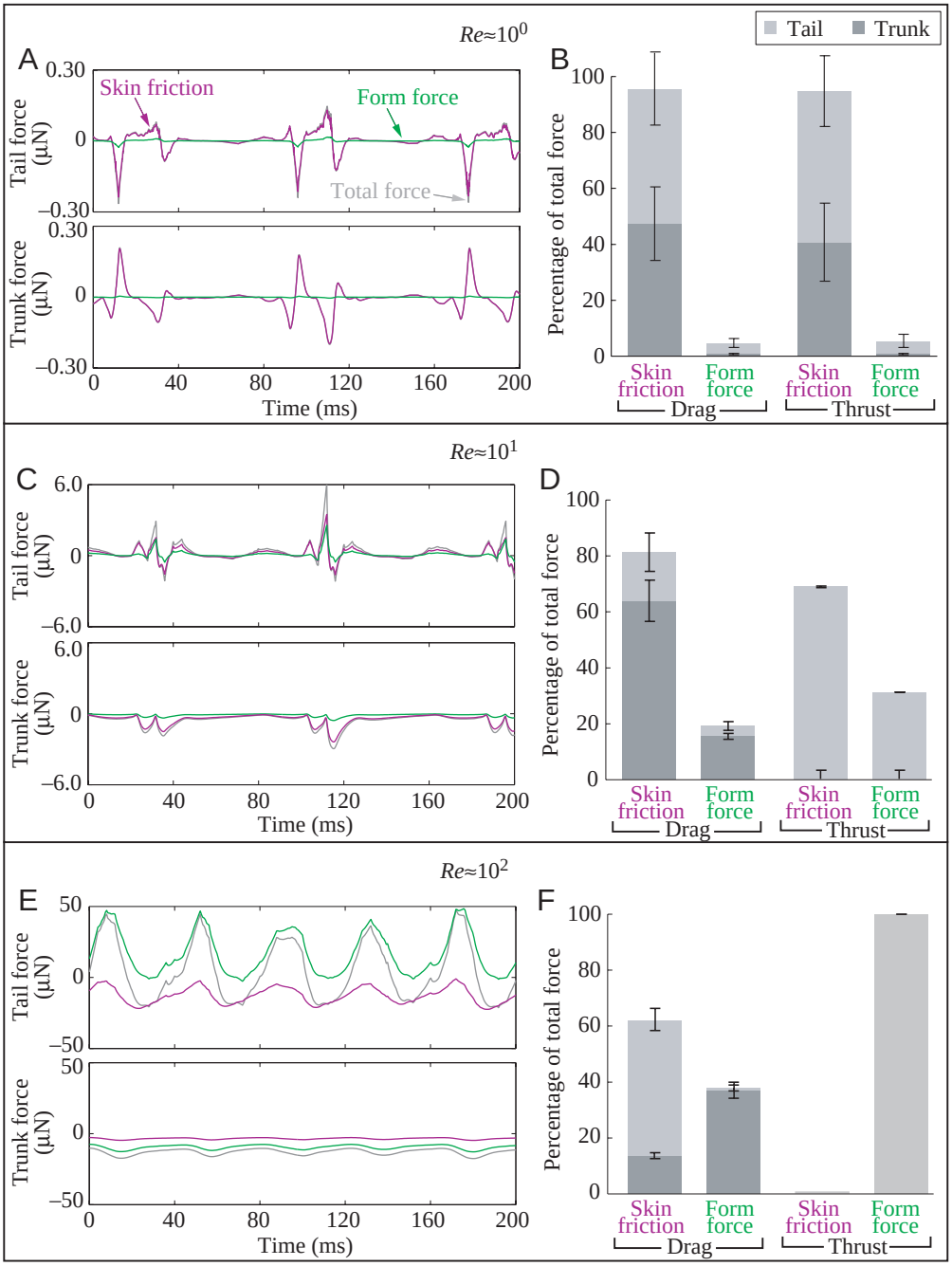

Fig. 8. Thrust and drag predicted by the quasi-steady model to act on the body of a freely swimming larva at different Reynolds numbers (*Re*). The graphs on the left (A,C,E) show a representative time series of the skin friction (violet lines) and form force (green lines) acting on the trunk and tail for approximately 4.5 tail beats with the same non-dimensional tail kinematics and different body lengths. Thrust acts in the positive direction and drag acts in the negative direction. The total force is the sum of skin friction and the form force. The graphs on the right (B,D,F) illustrate the percentage of the total thrust and drag that is generated by skin friction and form force that acts on the trunk and tail. Error bars denote ±1 S.D., which is variation generated by running simulations with different kinematic patterns (N=5). *Re* was varied by changing the body length of model larvae.

unsteady model better predicted the trajectory of swimming than did the quasi-steady model, which suggests that the acceleration reaction is important to undulatory swimming at intermediate *Re*.

This discrepancy between our results and Jordan (1992) on the relative importance of the acceleration reaction may be reconciled if the acceleration reaction coefficient varies with *Re*. The acceleration reaction is the product of the acceleration reaction coefficient (which depends on the height of the tail element), the density of water and the acceleration of a tail element (equation 12). Both Jordan (1992) and the present study used the standard inviscid approximation (equation 13) for the acceleration reaction coefficient (used in elongated body theory; Lighthill, 1975). However, chaetognaths attain $Re \approx 10^3$ and more rapid tail accelerations than ascidian larvae. If the actual acceleration reaction coefficient is lower than the inviscid approximation at the *Re* of ascidian larvae ($Re \approx 10^2$), then predictions of the acceleration reaction would be smaller in magnitude. The chaetognath may still generate sizeable acceleration reaction in this regime by beating its tail with relatively high accelerations.

Although swimming at $Re > 10^2$ has not been reported among ascidian larvae, numerous vertebrate and invertebrate species do swim in this regime. We predict that as *Re* approaches 10^3,

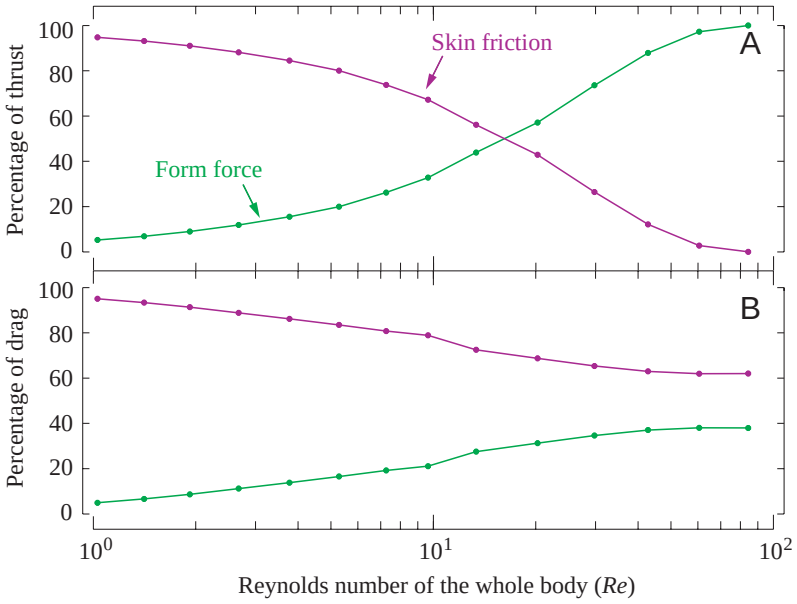

Fig. 9. The percentage of thrust and drag generated by skin friction and form force predicted by the quasi-steady model. Reynolds number of the whole body (*Re*) was varied by running a series of simulations over a range of body lengths. Lines show the percentage of (A) thrust and (B) drag generated by skin friction (violet) and form force (green).

the acceleration reaction contributes more to the generation of thrust in undulatory swimming. Although it remains unclear how the magnitude of the acceleration reaction changes with *Re*, the unsteady models proposed here ($\mathbf{F}=\mathbf{F}_f+\mathbf{F}_s+\mathbf{F}_a$) and elsewhere (Jordan, 1992; Vlyman, 1974) should approximate the hydrodynamics of undulatory swimming at $Re\approx10^3$.

Skin friction and form force

In support of prior work (e.g. Fuiman and Batty, 1997; Jordan, 1992; Vlyman, 1974; Webb and Weihs, 1986; Weihs, 1980), our quasi-steady model ($\mathbf{F}=\mathbf{F}_f+\mathbf{F}_s$) predicted that the relative magnitude of inertial and viscous forces is different at different *Re*. At $Re\approx10^0$, skin friction (acting on both the trunk and tail; Fig. 8) dominated the generation of thrust and drag (Fig. 9). This result is consistent with the viscous regime proposed by Weihs (1980) for swimming at $Re<10^1$. Also in accordance with Weihs (1980) are the findings that form force contributes more to thrust and drag at high *Re* than at low *Re* (Fig. 9) and that thrust (Fig. 8) is dominated by form force at $Re\approx10^2$. However, it is surprising that drag was generated more by skin friction than form force at $Re\approx10^2$ (Figs 8, 9). Contrary to Weihs' (1980) proposal for an inertial regime at $Re>2\times10^2$, this result suggests that the fluid forces that contribute to thrust are not necessarily the same forces that generate drag. This is unlike swimming in spermatozoa (at $Re\ll10^0$), where both thrust and drag are dominated by skin friction acting on both the trunk and flagellum (Gray and Hancock, 1955), or some adult fish (at $Re\gg10^2$), where thrust and drag are both dominated by the acceleration reaction (Lighthill, 1975; Wu, 1971).

Our results suggest that ontogenetic or behavioral changes in *Re* cause gradual changes in the relative contribution of skin friction and form force to thrust and drag. As pointed out by Weihs (1980), differences in intermediate *Re* within an order of magnitude generally do not suggest large hydrodynamic differences. Although it has been heuristically useful to consider the differences between viscous and inertial regimes (e.g. Webb and Weihs, 1986), it is valuable to recognize that these domains are at opposite ends of a continuum spanning three orders of magnitude in *Re*. This distinction makes it unlikely that larval fish grow through a hydrodynamic 'threshold' where inertial forces come to dominate the hydrodynamics of swimming in an abrupt transition with changing *Re* (e.g. Muller and Videler, 1996).

In summary, our results suggest that the acceleration reaction does not play a large role in the hydrodynamics of steady undulatory swimming at intermediate *Re* ($10^0<Re<10^2$). Our quasi-steady model predicted that thrust and drag are generated primarily by skin friction at low *Re* ($Re\approx10^0$) and that form force generates a greater proportion of thrust and drag at high *Re* than at low *Re*. Although thrust is generated primarily by form force at $Re\approx10^2$, drag is generated more by skin friction than form force in this regime. Unlike swimming at $Re>10^2$ and $Re<10^0$, the fluid forces that generate thrust cannot be assumed to be the same as those that generate drag at intermediate Reynolds numbers.

Table 3. *Reynolds numbers*

	Characteristic length (mm)	Reynolds number
Whole body	L=3.03±0.27	$Re=7.7\times10^1\pm2.3\times10^1$
Trunk	a=1.09±0.15	$Re_a=2.8\times10^1\pm1.0\times10^1$
Tail elements		
s=0.10L	s=0.23±0.01	$Re_{js}=1.1\times10^0\pm0.4\times10^0$
	l=0.41±0.02	$Re_{jl}=1.9\times10^0\pm0.7\times10^0$
s=0.30L	s=0.70±0.03	$Re_{js}=1.5\times10^1\pm0.5\times10^1$
	l=0.37±0.02	$Re_{jl}=7.8\times10^0\pm2.5\times10^0$
s=0.50L	s=1.18±0.06	$Re_{js}=5.7\times10^1\pm1.5\times10^1$
	l=0.29±0.02	$Re_{jl}=1.4\times10^1\pm0.4\times10^1$
s=0.70L	s=1.66±0.08	$Re_{js}=1.4\times10^2\pm0.3\times10^2$
	l=0.21±0.01	$Re_{jl}=1.7\times10^1\pm0.4\times10^1$
s=0.90L	s=2.16±0.10	$Re_{js}=2.4\times10^2\pm0.4\times10^2$
	l=0.12±0.01	$Re_{jl}=1.4\times10^1\pm0.2\times10^1$

L, body length; a, trunk length; s, distance along the tail from the tail base to the element; l, height of tail element; Re_a, Reynolds number of the trunk; Re, Reynolds number of the whole body; Re_{jl}, height-specific Reynolds number of a tail element; Re_{js}, position-specific Reynolds number of a tail element. N=14 for all measurements.

We thank M. Koehl for her guidance and advice, S. Sane for his wisdom on hydrodynamics, and A. Summers, W. Korff and W. Getz for their suggestions on the manuscript. This work was supported with an NSF predoctoral fellowship and grants-in-aid of research from the American Society of Biomechanics, Sigma Xi, the Department of Integrative Biology (U.C. Berkeley) and the Society for Integrative and Comparative Biology to M. McHenry. Additional support came from grants from the National Science foundation (# OCE-9907120) and the Office of Naval Research (AASERT # N00014-97-1-0726) to M. Koehl.

Appendix

Tether calibration

We used a least-squares method (described by Hill, 1996) to find the stiffness and damping constants of the tether from recordings of its position when allowed to oscillate without any larva attached. This method uses the equation of motion for the tether given any position measurement (φ_e):

$$c\frac{d\varphi_e}{dt} + k\varphi_e = -I_{tether}\frac{d^2\varphi_e}{dt^2} - m_{tether}\boldsymbol{g}h_{cm}\sin(\varphi_e)\,. \quad (29)$$

Moments generated at the pivot of the tether may be calculated with a version of this equation with different parameter values for each instant of time in a series of *e* position recordings. Such a time series of equations may be represented by the linear expression:

$$A\boldsymbol{q} = \boldsymbol{r}\,, \quad (30)$$

where

$$A = \begin{bmatrix} \frac{d\varphi_1}{dt} & \varphi_1 \\ \frac{d\varphi_2}{dt} & \varphi_2 \\ \vdots & \vdots \\ \frac{d\varphi_w}{dt} & \varphi_w \end{bmatrix},\quad \boldsymbol{q} = \begin{bmatrix} c \\ k \end{bmatrix},\quad \boldsymbol{r} = \begin{bmatrix} -m\boldsymbol{g}h_{cm}\sin(\varphi_1) - I\frac{d^2\varphi_1}{dt^2} \\ -m\boldsymbol{g}h_{cm}\sin(\varphi_2) - I\frac{d^2\varphi_2}{dt^2} \\ \vdots \\ -m\boldsymbol{g}h_{cm}\sin(\varphi_w) - I\frac{d^2\varphi_w}{dt^2} \end{bmatrix}. \quad (31)$$

Best fits for values of *c* and *k* were found by solving the following equation:

$$\boldsymbol{q} = (A^TA)^{-1}A^T\boldsymbol{r}\,, \quad (32)$$

where $(A^TA)^{-1}$ is the inverse of the product of *A* and the transpose of *A*. Solutions to this equation were found using MATLAB. This method was verified by analyzing fabricated position data that were generated by numerical solutions to equation 2 (a fourth-order Runge–Kutta in MATLAB) with known values of *k* and *c*.

Calculating tail force

The total force generated by the tail of a larva was calculated as the sum of forces acting on all elements of the tail. For example, the total acceleration reaction generated by the tail was found as the sum of acceleration reaction forces acting on tail elements:

$$\mathbf{F}_a = \sum_{j=1}^{n} \mathbf{E}_{ja}\,, \quad (33)$$

where *n* is the total number of tail elements. Similarly, the moment generated by these forces was calculated as the sum of cross products between the vector of the position of the tail element with respect to the body's center of mass ($\mathbf{R}_j$) and the acceleration reaction acting on tail elements (Meriam and Kraige, 1997b):

$$\mathbf{M}_a = \sum_{j=1}^{n} \mathbf{R}_j \times \mathbf{E}_{ja}\,. \quad (34)$$

The same calculations were used to determine the total force and moment generated by skin friction and form force for each instant of time in a swimming sequence.

List of symbols

a	length of the trunk
$\mathbf{A}$	acceleration of the body
$\mathbf{B}$	position of the center of mass
c_{ja}	added mass coefficient
c_{jf}	coefficient of force on tail element due to form force
$c_{j\,norm}$	coefficient of total force on tail element in the normal direction
c_{js}	coefficient of force on tail element due to skin friction
$c_{j\,s+f\,norm}$	coefficient of force on tail element in the normal direction due to form force and skin friction
$\mathbf{D}$	position of the center of volume of the trunk
$\mathbf{E}_j$	total force acting on a tail element
$\mathbf{E}_{ja}$	acceleration reaction on a tail element
$\mathbf{E}_{jf}$	form force on a tail element
$\mathbf{E}_{js}$	skin friction on a tail element
$\mathbf{F}$	total force generated by the tail
$\mathbf{F}_a$	tail force generated by acceleration reaction
$\mathbf{F}_f$	tail force generated by form force
$\mathbf{F}'_f$	tail force generated by form force in the direction of thrust
$\mathbf{F}_{inertia}$	tail inertia force
$\mathbf{F}_{norm}$	force in the normal direction measured on a plate
$\mathbf{F}_s$	tail force generated by skin friction
$\mathbf{F}'_s$	tail force generated by skin friction in the direction of thrust
$\boldsymbol{g}$	acceleration due to gravity
h_{cm}	distance from the tether pivot to the center of mass of the tether
$H_{f\,tail}$	percentage of thrust generated by form force on the tail
$h_{objective}$	distance from the tether pivot to the objective

h_{tip}	distance from the tether pivot to the tip of the pipette
i	volumetric element number
$\mathbf{I}$	inertia tensor for the body of a larva
$\mathbf{I}^{B}$	inertia tensor for the body in the body's coordinate system
I_{tether}	moment of inertia of the tether
j	tail element number
k_{damp}	damping coefficient
k_{f}	coefficient of the form force on the trunk
k_{spring}	spring coefficient
l	height of a tail element
L	body length
m_{body}	mass of the body of a larva
$\mathbf{M}$	total moment
$\mathbf{M}_{a}$	moment generated by the acceleration reaction
$\mathbf{M}_{f}$	moment generated by form force
$\mathbf{M}_{s}$	moment generated by skin friction
m_{tether}	mass of the tether
$\mathbf{O}$	moment generated by force on the trunk
p	speed of the trunk
P	tail-beat period
$\mathbf{P}$	velocity of the trunk
q	total number of volumetric elements
$\mathbf{R}_{j}$	position of the tail element with respect to the center of mass
Re	Reynolds number for whole body
Re_{a}	Reynolds number of the trunk
Re_{jl}	height-specific Reynolds number of a tail element
Re_{js}	position-specific Reynolds number for a tail element
r_{tether}	inner radius of the micropipette
s	distance along the tail from the tail base to the element
s_{j}	position of the element down the length of a tail
S	projected area of the trunk
t	time
$\mathbf{T}$	force acting on the trunk
$\mathbf{T}_{f}$	form force acting on the trunk
$\mathbf{T}_{s}$	skin friction acting on the trunk
$\overline{u}$	mean swimming speed
$\overline{v}$	mean tail element speed
$\mathbf{V}_{i}$	velocity of a tail element
$v_{j\,norm}$	speed of the normal component of the velocity of a tail element
$v_{j\,tan}$	speed of the tangent component of the velocity of a tail element
$\mathbf{V}_{j\,norm}$	normal component of the velocity of a tail element
$\mathbf{V}_{j\,tan}$	tangent component of the velocity of a tail element
x_{i}	x-coordinate of volumetric element
y_{i}	y-coordinate of volumetric element
z	position of inflection point along the length of the tail
α	amplitude of change in curvature
χ	amplitude of change in trunk angle
δ	linear deflection of the tether
Δs	width of a tail element
Δw_{i}	volume of a volumetric element
ε	wave speed of inflection point
φ	radial deflection of the tether at its pivot
φ_{e}	measurement of tether deflection
γ	period of change in curvature
κ	tail curvature
μ	dynamic viscosity of water
θ	trunk angle
ρ	density of water
ρ_{body}	density of tissue
Ω	rate of rotation about the center of mass
ζ	phase lag of inflection point relative to trunk angle
*	non-dimensional quantity

References

Batchelor, G. K. (1967). *An Introduction to Fluid Dynamics*. New York: Cambridge University Press.

Bone, Q. (1992). On the locomotion of ascidian tadpole larvae. *J. Mar. Biol. Ass. UK* **72**, 161-186.

Brackenbury, J. (2002). Kinematics and hydrodynamics of an invertebrate undulatory swimmer: the damsel-fly larva. *J. Exp. Biol.* **205**, 627-639.

Cloney, R. A. (1987). Phylum Urochordata, Class Ascidiacea. In *Reproduction and Development of Marine Invertebartes of the Northern Pacific Coast* (ed. M. F. Strathmann), pp. 607-646. Seattle: University of Washington Press.

Daniel, T., Jordan, C. and Grunbaum, D. (1992). Hydromechanics of Swimming. In *Advances in Comparative and Environmental Physiology*, vol. 11 (ed. R. McN. Alexander), pp. 17-49. London: Springer-Verlag.

Daniel, T. L. (1984). Unsteady aspects of aquatic locomotion. *Am. Zool.* **24**, 121-134.

Dickinson, M. H. (1996). Unsteady mechanisms of force generation in aquatic and aerial locomotion. *Am. Zool.* **36**, 537-554.

Dickinson, M. H., Farley, C. T., Full, R. J., Koehl, M. A. R., Kram, R. and Lehman, S. (2000). How animals move: an integrative view. *Science* **288**, 100-106.

Dickinson, M. H., Lehmann, F.-O. and Sane, S. P. (1999). Wing rotation and the aerodynamic basis of insect flight. *Science* **284**, 1954-1960.

Fuiman, L. A. and Batty, R. S. (1997). What a drag it is getting cold: partitioning the physical and physiological effects of temperature on fish swimming. *J. Exp. Biol.* **200**, 1745-1755.

Granger, R. A. (1995). *Fluid Mechanics*. New York: Dover.

Grave, C. (1934). The Botryllus type of ascidian larva. *Pap. Tortugas Lab.* **28**, 143-156.

Grave, C. and Woodbridge, H. (1924). *Botryllus schlosseri* (Pallas): the behavior and morphology of the free-swimming larva. *J. Morph.* **39**, 207-247.

Gray, J. and Hancock, G. J. (1955). The propulsion of sea-urchin spermatozoa. *J. Exp. Biol.* **32**, 802-814.

Gray, J. and Lissmann, H. W. (1964). Locomotion of nematodes *J. Exp. Biol.* **41**, 135-154.

Hill, R. O. (1996). *Elementary Linear Algebra*. Philadelphia: Saunders College Publishing.

Hoerner, S. F. (1965). *Fluid-Dynamic Drag*. Brick Town, NJ: Hoerner Fluid Dynamics.

Jordan, C. E. (1992). A model of rapid-start swimming at intermediate Reynolds number: undulatory locomotion in the chaetognath *Sagitta elegans*. *J. Exp. Biol.* **163**, 119-137.

Lamb, H. (1945). *Hydrodynamics*. New York: Dover.

Lighthill, J. (1975). *Mathematical Biofluidynamics*. Philadelphia: Society for Industrial and Applied Mathematics.

McHenry, M. J. (2001). Mechanisms of helical swimming: asymmetries in the morphology, movement and mechanics of larvae of the ascidian *Distaplia occidentalis*. *J. Exp. Biol.* **204**, 2959-2973.

McHenry, M. J. and Strother, J. A. (in press). The kinematics of phototaxis in larvae of the ascidian *Aplidium constellatum*. *Mar. Biol.*

Meriam, J. L. and Kraige, L. G. (1997a). *Dynamics*. New York: John Wiley & Sons.

Meriam, J. L. and Kraige, L. G. (1997b). *Statics*. New York: John Wiley & Sons.

Muller, U. K. and Videler, J. J. (1996). Inertia as a 'safe harbor': do fish larvae increase length growth to escape viscous drag? *Rev. Fish Biol. Fish.* **6**, 353-360.

Nauen, J. C. and Shadwick, R. E. (1999). The scaling of acceleratory aquatic locomotion: Body size and tail-flip performance of the California spiny lobster *Panulirus interruptus*. *J. Exp. Biol.* **202**, 3181-3193.

Pennington, J. T. and Emlet, R. B. (1986). Ontogenetic and diel vertical migration of a planktonic echinoid larva, *Dendraster excentricus* (Eschscholtz): occurrence, causes, and probable consequences. *J. Exp. Mar. Biol. Ecol.* **104**, 69-95.

Russ, J. C. (1999). *The Image Processing Handbook*. Boca Raton, FL: CRC Press.

Sane, S. P. and Dickinson, M. H. (2001). The control of flight force by a flapping wing: lift and drag production. *J. Exp. Biol.* **204**, 2607-2626.

Sane, S. P. and Dickinson, M. H. (2002). The aerodynamic effects of wing rotation and a revised quasi-steady model of flapping flight. *J. Exp. Biol.* **205**, 1087-1096.

Schlichting, H. (1979). *Boundary-Layer Theory*. New York: McGraw-Hill.

Shampine, L. F. and Gordon, M. K. (1975). *Computer Solution of Ordinary Differential Equations: The Initial Value Problem*. San Francisco: W. H. Freeman & Co.

Sokal, R. R. and Rohlf, F. J. (1995). *Biometry*. New York: W. H. Freeman & Co.

Symon, K. R. (1960). *Mechanics*. Reading, MA: Addison-Wesley.

Vlyman, W. J. (1974). Swimming energetics of the larval anchovy, *Engraulis mordax*. *Fish. Bull.* **72**, 885-899.

Vogel, S. (1981). *Life in Moving Fluids*. Princeton: Princeton University Press.

Webb, P. W. and Weihs, D. (1986). Functional locomotor morphology of early life-history stages of fishes. *Trans. Am. Fish. Soc.* **115**, 115-127.

Weihs, D. (1974). Energetic advantages of burst swimming of fish. *J. Theor. Biol.* **48**, 215-229.

Weihs, D. (1980). Energetic significance of changes in swimming modes during growth of larval achovy, *Engraulis mordax*. *Fish. Bull.* **77**, 597-604.

White, F. M. (1991). *Viscous Fluid Flow*. New York: McGraw-Hill.

Williams, T. A. (1994). Locomotion in developing *Artemia* larvae: mechanical analysis of antennal propulsors based on large-scale physical models. *Biol. Bull* **187**, 156-163.

Wu, T. Y. (1971). Hydromechanics of swimming propulsion. Part 2. Some optimum shape problems. *J. Fluid Mechanics* **46**, 521-544.